CORA Cork Open Research Archive
Cartlann Taighde Oscailte Chorcaí

Title	Honeycomb micro/nano-architecture of stable ß-NiMoO4 electrode/catalyst for sustainable energy storage and conversion devices
Authors	Padmanathan, Narayanasamy;Shao, Han;Razeeb, Kafil M.
Publication date	2020-08-30
Original Citation	Padmanathan, N., Shao, H. and Razeeb, K. M. (2020) 'Honeycomb micro/nano-architecture of stable Î²-NiMoO4 electrode/ catalyst for sustainable energy storage and conversion devices', International Journal of Hydrogen Energy, 45(55), pp.30911-30923. https://doi.org/10.1016/j.ijhydene.2020.08.058
Type of publication	Article (peer-reviewed)
Link to publisher's version	10.1016/j.ijhydene.2020.08.058
Rights	© 2020, Elsevier B.V. All rights reserved. This manuscript version is made available under the CC BY-NC-ND 4.0 license. - https://creativecommons.org/licenses/by-nc-nd/4.0/
Download date	2026-11-07 11:16:06
Item downloaded from	https://hdl.handle.net/10468/10488

UCC
University College Cork, Ireland
Coláiste na hOllscoile Corcaigh

Honeycomb micro/nano-architecture of stable β-$NiMoO_4$ electrode/catalyst for sustainable energy storage and conversion devices

N. Padmanathan[a,b], Han Shao[a] and Kafil M. Razeeb[a*]

[a]*Micro-Nano Systems Centre, Tyndall National Institute, University College Cork, Dyke Parade, Lee Maltings, Cork T12 R5CP, Ireland*

[b]*Department of Physics, Karpagam Academy of Higher Education, Coimbatore – 641021, Tamilnadu, India.*

***Corresponding Author**: kafil.mahmood@tyndall.ie

Abstract:

Multi-functionality is a highly desirable feature in designing new electrode material for both energy storage and conversion devices. Here, we report a well-integrated and stable β-$NiMoO_4$ that was fabricated on three dimensional (3D) nickel foam (NF) by a simple hydrothermal approach. The obtained β-$NiMoO_4$ with interesting honeycomb like interconnected nanosheet microstructure leads to excellent electrochemical activity. As an electrode for Supercapatteries, β-$NiMoO_4$–NF showed a high specific capacity of 178.2 $mAhg^{-1}$ (916.4 F g^{-1}) at 5 $mAcm^{-2}$ current density. Most importantly, the fabricated symmetric device exhibits a maximum specific energy of 35.8 $Whkg^{-1}$ with the power output of 981.56 Wkg^{-1} and excellent cyclic stability. In methanol electro-oxidation, the β-$NiMoO_4$ –NF catalyst deliver the high current density of 41.8 $mAcm^{-2}$ and much lower onset potential of 0.29 V with admirable long term stability. Apart from the above electrochemical activity, the β-$NiMoO_4$ –NF honeycomb microstructure demonstrates a promising non-noble electrocatalyst for oxygen evolution reaction (OER) and hydrogen evolution reaction (HER) and showed a considerable overpotential of 351 mV (OER) and 238 mV (HER). The attractive multifunctional electrochemical activity of β-$NiMoO_4$–NF could be originates from their unique honeycomb micro/nano structure which can acts as an "ion reservoir" and thus leads to superior energy storage and conversion processes.

Keywords: Electrode, Supercapatteries, Electro-oxidation, Specific capacity, Overpotential

1. Introduction

Our modern society is currently facing an energy crisis and environmental problems due to the rapid depletion of fossil fuels and global warming [1]. In order to overcome these

complications there is an urgent demand for sustainable energy storage and conversion devices [2]. In this regard, systems of electrochemical energy storage and conversion such as Li-ion batteries [3, 4], electrochemical capacitors [5, 6], Supercapatteries [7, 8] and fuel cells [9, 10] have been particularly developed. Recently, Supercapatteries [11-13] and direct methanol fuel cell (DMFC) [14-16] have been regarded as a promising clean energy storage and conversion device. Besides their various applications in the fields of portable electronic products [17], hybrid electric vehicles [18, 19], and smart electrical grids [20], they have many attractive features of low pollutant emission, higher energy efficiency and ease of operation [21]. The capability of the energy storage and the conversion efficiency is mainly governed by the electrode materials, which directly participate in to electrochemical reaction or indirectly catalyse electro-oxidation of fuels [22]. Therefore, designing an appropriate electrode is essential to achieve high storage capacity and great rate of conversion with low onset potential. So far, RuO_2 and traditional carbon materials are adopted for industry-scale production of supercapacitor, while expensive platinum alloy is used in fuel cells [23-25]. However, commercial challenge associated with these electrode/catalyst materials limits their large scale applications. Thus many efforts have been devoted fabricate low cost transition metal oxides (i.e. NiO, Co_3O_4 MnO_2, $NiCo_2O_4$ etc.,) to replace the traditional and expensive electrode/catalyst materials [26, 27]. Unfortunately, the inadequate electron transfer kinetics and catalytic activity of these metal oxides hinders their usefulness in these applications. Hence, new alternative transition metal oxides are needed, which possess superior ion/electron transport for charge storage and negligible CO poisoning effect towards methanol oxidation. Thereby, the current research interest is focusing towards the exploration of dual-functional, active and advanced electrode materials that can store enough energy and energy conversion with highest current density.

In recent years ternary metal oxides having two different metal cations received huge interest due to their superior performance for energy related applications. In particular the bimetallic oxides with the ABO_4 structure in which A and B represents different metal cations (A = Ni, Co, Mn, Zn and B = Mo, W) are investigated for energy storage and conversion devices [28, 29]. Among them, $NiMoO_4$ is a low cost and abundant material with high electrical conductivity when compared to their mono-metallic oxides [30]. This higher conductivity is of benefit to the rapid electron/ion transport in an electrode. $NiMoO_4$ also contains highly oxidized redox couples Ni^{2+}/Ni^{3+}, which are known as active centre for electro-oxidation/reduction reactions. Thereby, it has been investigated as the electrode for methanol

oxidation, supercapacitor and lithium ion batteries [31-33]. Peng et al. fabricated $NiMoO_4$ on various conducting substrates and proposed as advanced electrodes for asymmetric supercapacitor [34]. Recently, controlled morphology of $NiMoO_4$ nanostructures and $NiMoO_4$/carbon nanocomposites were investigated for supercapacitor application [35, 36]. Meanwhile, several different types of metal oxide nanostructures including nanosheets, nanospheres, nano-needles and nanowires have been fabricated on three dimensional (3D) nickel foam (NF) and investigated for direct methanol oxidation in alkaline medium. [37, 38]. Recently, the electrocatalytic activity of $NiMoO_4$ through phosphorization process [39] and CeO_2 modified $NiMoO_4$ nanosheet arrays towards urea oxidation were examined [40]. It is interesting to point out that $NiMoO_4$ is stable in both α-$NiMoO_4$ and β-$NiMoO_4$ phases with same monoclinic crystal structure and greatly influence the structure-property relation [41-45]. It has been proven that β-$NiMoO_4$ has three times higher intrinsic catalytic activity than the α-$NiMoO_4$ [43, 44]. So, the formation of stable β-$NiMoO_4$ is desirable for electrochemical applications. Moreover, it has been well-established that the electrochemical performances of devices are directly affected by the intrinsic properties and micro/nano structure of the electrode [45]. To date, mostly α-$NiMoO_4$ phase with distinct microstructure has been investigated for different applications. To the best of our knowledge, there is no reports available on β-$NiMoO_4$ grown directly on 3D nickel foam for electro-oxidation of methanol and need to explore further to utilize this material for device fabrication.

Here, we propose a simple hydrothermal approach to fabricate β-$NiMoO_4$ nanosheet arrays with honeycomb structure on a porous NF and investigated its usability as electrode for supercapattery and methanol oxidation. This binder free β-$NiMoO_4$-NF was directly used as electrodes for the supercapattery and as catalyst for methanol oxidation in alkaline environment. When used as electrodes for supercapattery, the symmetric device delivered a high specific energy and power with long cyclability. The porous network structure provides rapid electron/ion and methanol transport during the electrochemical process. Electro-oxidation tests demonstrated desired methanol conversion performance including high peak current (41.78 $mAcm^{-2}$), superior long-term cyclic stability and resistivity against carbon deposition. Furthermore, the evaluation of this catalyst for oxygen and hydrogen evolution reactions demonstrated that β-$NiMoO_4$-NF can be a versatile bifunctional electrode with significant catalytic performance.

2. Experimental

2.1 Fabrication of β-$NiMoO_4$ on NF

Analytical grade reagents were used to fabricate $NiMoO_4$ over NF substrate. The growth of $NiMoO_4$ on 3D-NF is a two-step process. Initially, the NF (~99.9%, Shanghai Tankii Alloy Material Co. Ltd, China) was cleaned with concentrated HCl (~ 36%, Sigma Aldrich, UK) and ethanol by sonication for 30 min each. The pre-treated NF was dried with N_2 gas and kept in vacuum desiccator. Then, equal molar ratio (1:1) of $Ni(NO_3)_2.6H_2O$ (~99.9%, Sigma Aldrich, UK) and $Na_2MoO_4 \cdot 2H_2O$ (~99.9%, Sigma Aldrich, UK) were dissolved in deionized (DI) water. Following this, appropriate amount of carbamide (~99.9%, Sigma Aldrich, UK) was added to the above mixed solution under constant stirring. Finally, 0.1 g of Polyvinyl Pyrrolidone (PVP Mw~40000, ~99.9%, Alfa Aesar, UK) was added to the solution before pour into autoclave. The homogenously mixed solution was transferred to teflonated stainless steel autoclave, which contains pre-treated NF (3 × 3 cm) and was kept at 180 ºC for 12 h. After the hydrothermal treatment, $NiMoO_4$ coated NF was taken off from the container and washed several times with DI water, ethanol and acetone consecutively to remove any impurities. In order to increase the crystalline nature, the as deposited NF was calcined in air at 450 ºC with the heating rate of 5 ºC/min for 2 h and then directly used as electrodes and anode for supercapatteries and methanol electro-oxidation in alkaline environment.

2.2 Characterization

The crystal structure and phase of the β-$NiMoO_4$-NF were characterized by Powder X-ray diffraction (XRD) technique (Philips PW3710-MPD diffractometer) with the CuKα radiation (λ=1.5403Å). The internal chemical structure of the catalyst was studied from Raman spectra, recorded using the Renishaw (RA 100) in via confocal Raman Microscope at 514.5 nm excitation. The surface morphology and atomic composition of the sample were examined by a field emission scanning electron microscope (FEI QUANTA 650 HRSEM) and energy dispersive X-ray spectrometer (EDX Oxford Instruments INCA energy system), respectively. A transmission electron microscope (JEOL HRTEM-2100 at 200 kV) was used to understand the microstructure. In order to investigate the energy storage and conversion capability of the prepared sample, Cyclic Voltammetry (CV), Linear Sweep Voltammetry (LSV), Chronopotentiometry (CP), Chronoamperometry (CA) and Electrochemical Impedance Spectroscopy (EIS) techniques were used using a electrochemical workstation (CHI 660D, USA). A three-electrode ($NiMoO_4$-NF as working (1 × 1 cm^{-2}), platinum wire as counter and

saturated calomel as reference electrodes (SCE)) system was employed for the electrochemical studies where, 3 M KOH was used as the electrolyte. Typical mass loading of the working electrode is ~2 mg cm^{-2}. The symmetric supercapattery cell was fabricated with two $NiMoO_4$/NF electrodes at equal mass ratio (1:1 mg), which were separated by a Celgard separator (Battery grade, Sigma Aldrich, UK). EIS was recorded in the frequency range from 100 Hz to 100 KHz at open circuit potential. For methanol oxidation reaction (MOR), Oxygen evolution reaction (OER) and Hydrogen evolution reaction (HER), $NiMoO_4$-NF (1 × 1 cm^{-2}) was directly applied as a working catalyst and evaluated in 1 M KOH solution with and without addition of 1 M CH_3OH.

3. Results and discussion

3.1 XRD and Raman Analysis

Phase and crystal structure of the as prepared $NiMoO_4$/NF are characterized using powder XRD techniques and shown in Fig. S1 (Supplementary Information (SI)). There is no visible diffraction pattern observed for $NiMoO_4$ except the NF peak as indexed. This result indicates the formation of less crystalline (nearly amorphous) $NiMoO_4$ over NF surface. To confirm further, the Powder XRD pattern was taken for the sample collected during hydrothermal process after 450 ºC heat treatment and displayed in Fig. 1(a). It can be indexed to the β-$NiMoO_4$ with monoclinic crystal structure and C2/m space group. The observed diffraction peaks are in good agreement with the standard JCPDS card no. 45-0142 [46]. Intense diffraction peak at 27.9º indicates the characteristic (2 2 0) orientation of β-$NiMoO_4$. No secondary phases such as NiO or MoO_3 were found in the XRD pattern, which infers the formation of phase pure compound. Figure 1(b) shows the Raman spectrum of $NiMoO_4$ grown over NF. The high intensity peak at 936 cm^{-1} demonstrates that formation of β-$NiMoO_4$, whereas the major peak should be observed at 961 cm^{-1} for α-$NiMoO_4$ [46-48]. The observed low intensity peaks at 880, 816, and 366 cm^{-1}also supports the growth of β-$NiMoO_4$ [48]. Typical Raman peak at 936 and 880 cm^{-1} correspond to the symmetric and asymmetric stretching modes of the Mo-O bonds [47]. Whereas the other peaks at 816 and 366 cm^{-1} might be associated to the Ni-O-Mo asymmetric stretching and Mo-O bending modes, respectively [46]. The Ni-O vibration mode at 539 cm^{-1} reveals the surface oxidation of NF substrate. The detected Raman peak substantiates the growth of β -$NiMoO_4$ and in agreement with the XRD results.

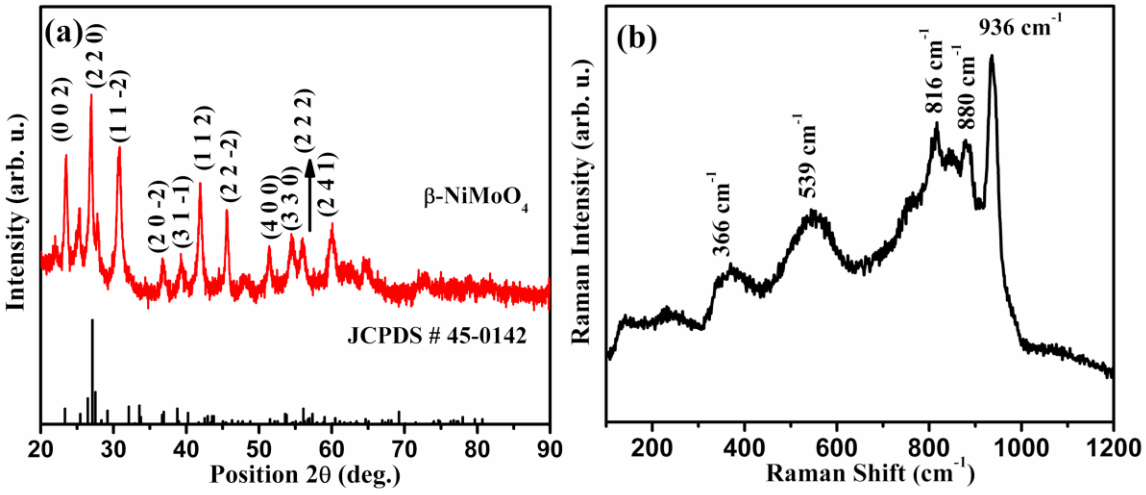


Fig. 1 (a) XRD pattern of β -$NiMoO_4$ (powder) and (b) Raman spectrum of β -$NiMoO_4$-NF.

3.2 Morphological Studies

Figure 2(a-c) shows the FESEM images of the β-$NiMoO_4$ on NF. The low magnification image (Fig. 2a) clearly evidences the formation of interconnected nanosheets and honeycomb-like morphology with open voids. In close view, high magnification SEM images (Fig 2(b & c)) shows the well-interconnected nanosheets with uniform voids of ~1.1 μm. Typical thickness of the nanosheets is found to be 18 nm. To better understand the honeycomb like architecture, TEM analysis was carried out for the sample scratched off from the NF and the representative images of β-$NiMoO_4$ are shown in Fig. 2(d-f). The images reveal well-connected thin nanosheets. Figure 2(f) displays the selected area electron diffraction (SAED) pattern of β-$NiMoO_4$ and shows dispersed spots with diffused rings demonstrating the poor crystallinity. This result is matched with the observed XRD pattern as discussed earlier. The EDS spectrum (Fig S2 in SI) shows the presence of Ni, Mo and O without any impurities.

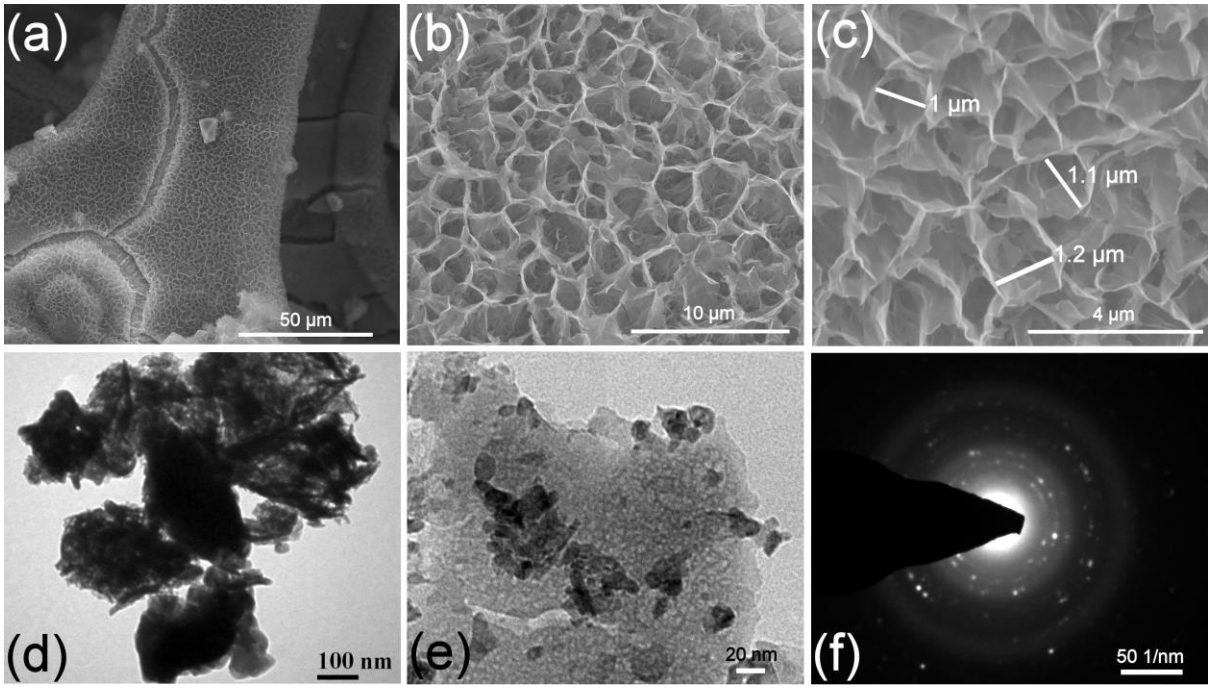


Fig. 2 (a-c) HRSEM images of β -$NiMoO_4$-NF at different magnifications, (d-e) TEM images β -$NiMoO_4$ (scratched from NF) and (d) the corresponding SAED pattern.

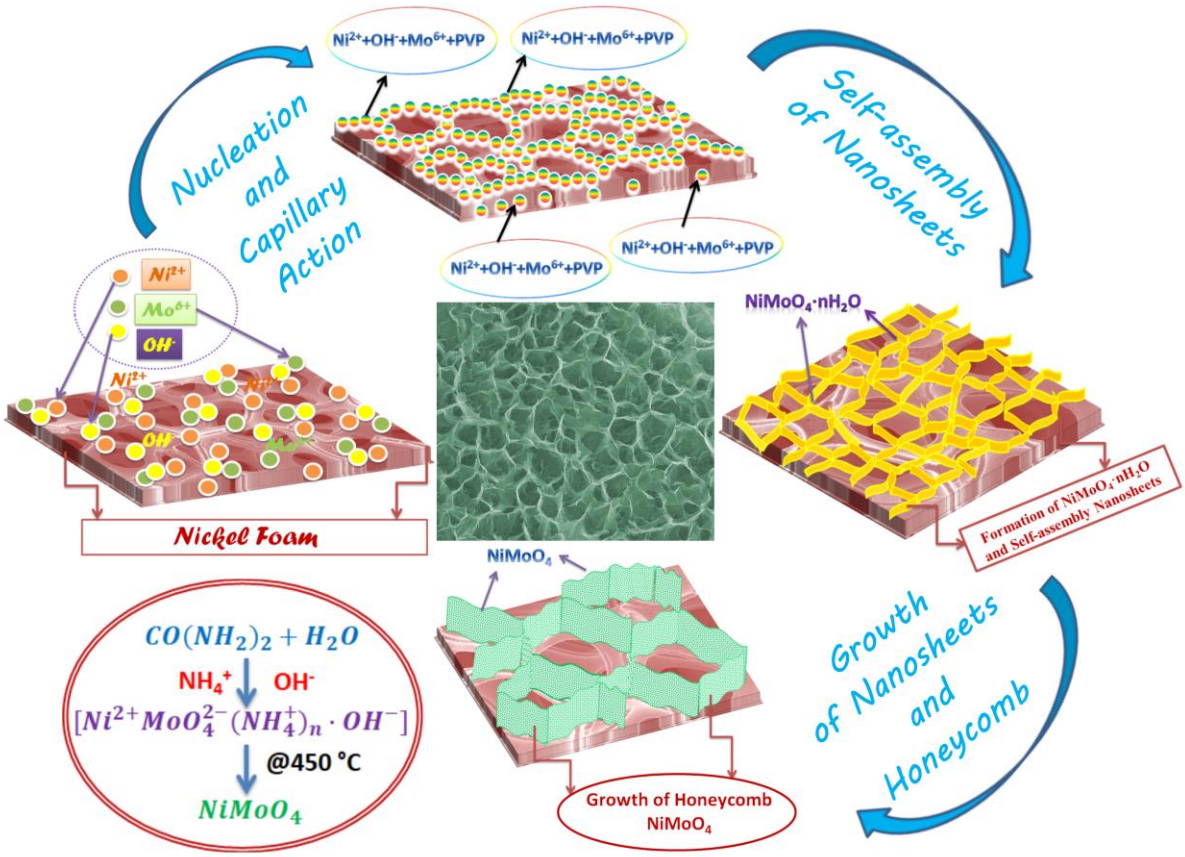


Fig. 3 Schematic representation of $NiMoO_4$ honeycomb micro/nano structure growth process.

The growth of this interesting microstructure may be due to the controlled OH^- ion driven by capillary force in the solution during hydrothermal process. The proposed growth process is illustrated in Fig. 3. The presence of PVP, interconnects the formed nanosheets to make honeycomb architecture based on the solid-liquid interface reaction mechanism. During heat treatment, the releases of CO_2, NH_3 and CO introduce more open space, which could form the uniform nanosheets without destructing the honeycomb network structure. Typical hydrothermal reaction mechanism is represented as in equations (1) – (3):

$$CO(NH_2)_2\ (excess) + nH_2O \rightarrow nNH_4^+ + OH^- + CO_2 \uparrow \quad (1)$$

$$Ni^{2+} + MoO_4^{2-} + nNH_4^+ + OH^- \rightarrow [Ni^{2+}MoO_4^{2-}(NH_4^+)_n \cdot OH^-] \quad (2)$$

$$[NiMoO_4 \cdot nH_2O] \rightarrow NiMoO_4 + nH_2O \quad (3)$$

Initially, the urea hydrolysis into ammonium hydroxide and it will form the complex when reacting with the nickel and molybdenum ions as in equation (2). It is well known that the urea plays an active role in hydrothermal approach by influencing the morphology of the product as well as phase transition [48]. The formation of β-phase can be readily explained by the presence of excess urea in the reaction bath. During the crystallization process, the ammonium ion decomposes to NH_3 and H^+ and results in the formation of hydrated nickel molybdate [49]. Finally, loss of NH_3 and H_2O leads to the growth of β-$NiMoO_4$ honeycomb architecture over NF after calcination at 450 °C [50]. At hydrothermal condition, urea releasing OH^- ions which increase the solution pH slowly for $NiMoO_4$ nucleation process and further growth of nanosheets occurs by Oswald ripening phenomenon [51]. The extended hydrothermal treatment leads to an oriental attachment of the nanosheets and the orientation can be linked to the PVP at the solid-liquid interface [52]. Thereby, uniform honeycomb like microstructure is formed.

3.3 Electrochemical Analysis

3.3.1 Energy Storage Studies

The β-$NiMoO_4$ nanosheet arrays integrated on NF was directly used as an electrode for supercapatteries. Cyclic voltammetry (CV) and chronopotentiometry (CP) techniques have been used to evaluate the initial electrode activity in 3 M KOH using a three electrode system.

Fig. 4(a) shows the cyclic voltammetry curves of β-$NiMoO_4$-NF electrode at different scan rates ranging from 1 – 50 mVs^{-1}. The redox peaks displays faradaic type energy storage behaviour unlike supercapacitor or pseudocapacitor, which usually have the ideal rectangular CV response. The peak current increases with the scan rate reveal the surface redox reaction at the electrode/electrolyte interface. The redox reaction is mainly originating from the Ni^{2+}/Ni^{3+} conversion. While, the Mo could leads to increasing the electrical conductivity and thus enhance the specific capacity, there is no direct contribution of Mo^{6+} to redox process because of their limited potential window [53]. The CVs are nearly symmetric and the observed peak currents are quite comparable in both forward and reverse sweeps, indicating good reversibility of the redox process. It is noteworthy that the anodic and cathodic peak potential shift towards positive and negative respectively, as the scan rate increases from 1 to 50 mV s^{-1}. This may be due to the high ohmic resistance, slow electron kinetics, and low ionic diffusivity of the battery type electrode [54]. The anodic peak current vs. square root of scan rate plot is shown in Fig. S3(a). It shows a linear relationship, confirming a diffusion controlled rather than absorption controlled electrochemical reaction [55]. To understand the actual redox mechanism Power law was used [56]. According to Power law, the peak current can be related to the following equation: $i_{pa} = av^b$, where i_{pa} is the anodic peak current, v is the scan rate and a, b are the adjustable parameters. The b value can be extracted from the $log\ i_{pa}$ vs. $log\ v$ plot as shown in Fig. S3(b) where, the slope should be close to 0.5 for diffusion controlled battery type redox process [57]. From the plot, a slope of 0.61 is suggesting a dominant battery type charge storage and less capacitive storage. The amount of charge stored by the faradaic process can be evaluated by the equations (4) and (5): [55-57]:

$$i_{pa} = s_1 v + s_2\sqrt{v} \qquad (4)$$

$$\frac{i_{pa}}{\sqrt{v}} = s_1\sqrt{v} + s_2 \qquad (5)$$

Where i_{pa} is the anodic peak current, and $s_1 v$ & $s_2\sqrt{v}$ are the respective capacitive and faradaic current contributions during redox process. The corresponding plot between $\frac{i_{pa}}{\sqrt{v}}$ and $\sqrt{v}$ at peak potential is shown in Fig. S3(c). From the slope and intercept, s_1 and s_2 values can be obtained and are found to be 11.47 and 1.142, respectively. The contribution of faradaic and capacitive current in total integrated charge storage of the electrode is shown in Fig. S3(d). It can be seen that the diffusion controlled kinetics (i.e. battery type current) dominates over capacitive kinetics in this honeycomb β-$NiMoO_4$-NF electrode. While the scan rate increases

≥ 30 mVs^{-1}, the capacitive current has increased significantly, this further indicates the contribution of capacitive charge storage [58]. At the lower scan rates, the electrolyte ions can diffuse into core active sites and thus battery type intercalation current dominates. The open networked honeycomb microstructure and a robust mechanical integrity with NF, provides more active sites for redox reaction. Whereas at the high scan rates, diffusion process slow down due to the limited access of inner active sites [54]. From this observation it can be concluded that the β-$NiMoO_4$-NF electrode exhibits both battery type and capacitive charge storage features and thereby may be a promising positive electrode for the supercapatteries.

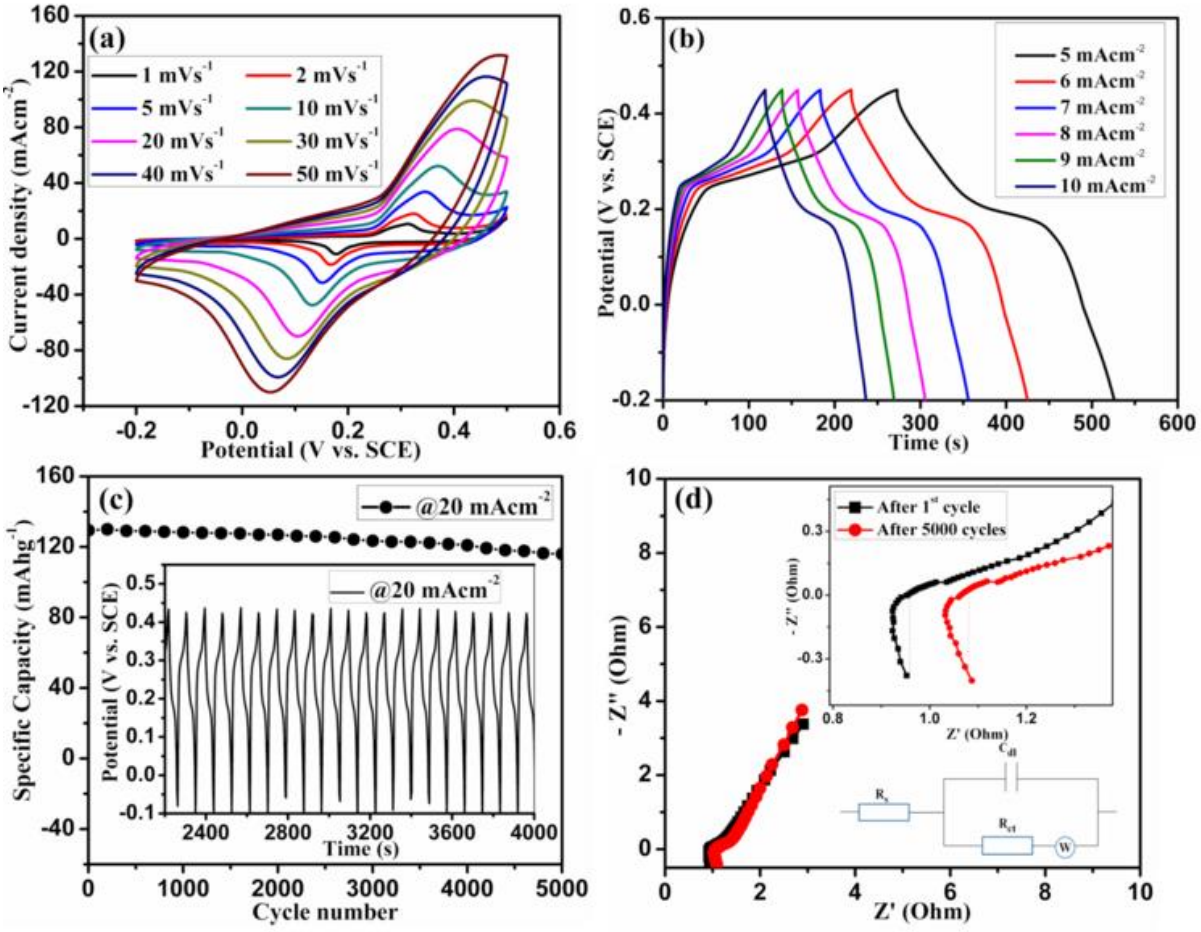


Fig.4 (a) CV curves of β-$NiMoO_4$-NF at different scan rate, (b) Charge/discharge profile at various current densities, (c) Cyclic stability of the electrode and (d) EIS spectra of the electrode after 1st and 5000 cycles.

For a better evaluation of β-$NiMoO_4$-NF for supercapattery application, chronopotentiometry analysis was carried out in the voltage range of -0.2 to 0.45 V at various current densities ranging from 5 to 50 $mAcm^{-2}$. Fig. 4(b) shows the charge/discharge profile of the β-$NiMoO_4$-NF electrode at low current densities of 5-10 $mAcm^{-2}$ whereas, Fig. S4(a) shows

the profile at high current densities (15-50 $mAcm^{-2}$). At all the measured current densities, the charge/discharge profiles displays battery-type charge storage behaviour and is in good agreement with the CV results.. The bare nickel foam has only a small contribution in the total specific capacity, which could be neglected. At low current density (5 $mAcm^{-2}$), the discharge time is quite large, indicating that the electrolyte ions had enough time to reach core active sites. Whereas, at high current density (50 $mAcm^{-2}$), the electrolyte possess time constraints to reach core active region, which limits the ion transport [53]. Since the electrode mechanism is dominated by battery-type behaviour, the specific capacity (in $mAhg^{-1}$) can be determined using equation (6) [59]:

$$C_s = \frac{I \times t}{3600 \times m} \qquad (6)$$

where, I is the charge-discharge current (mA), t is the discharge time (s) and m is the mass loading of the active material (g). The specific capacity values against the applied current densities are illustrated in Fig. S4(b), where a capacity of 178.2, 164.4, 129.4, and 94.4 $mAhg^{-1}$ is achieved for 5, 10, 20, and 50 $mAcm^{-2}$, respectively. As observed in Fig. S4(b), the specific capacity decreases gradually with increasing current density and may be due to the limited electrolyte ion diffusion into core level of active materials at a higher current density. At a maximum current density of 50 $mAcm^{-2}$ (10 fold increase), 52% specific capacity has been retained from its initial capacity, suggesting a good rate capability for this electrode. To avoid the confusion during comparison, the measured specific capacity values are also represented in terms of specific capacitance and are 916.4, 845.7, 665.7 and 485.7 Fg^{-1} for the same current densities as mentioned above. The specific capacity of this electrode is better than the other supercapattery electrodes reported so far, such as $NiMoO_4$/Carbon nanocomposite grown on NF with different morphology (805 Fg^{-1} @ 1 Ag^{-1}) [35] and NiMoO4/$CoMoO_4$ hybrid electrode, which shows a maximum specific capacitance of 740 Fg^{-1} at a 1 Ag^{-1} current density [36]. Meantime, $NiMoO_4$ nanostructure on stainless steel substrate (61.8 $mAhg^{-1}$ at 1 Ag^{-1}) [60], hydrangea-type Bi_2MoO_6 (485 Fg^{-1} at 5 Ag^{-1}) [54], NiF_2@Ni nano arrays (51 Fcm^{-2} at 1 mVs^{-1}) [55] and hetero-structured $Ni(OH)_2/CuCo_2S_4$/Ni networks (749 $\mu Ahcm^{-2}$ at 1 $mAcm^{-2}$) [58]. A good cyclic stability is an important factor for real device fabrication. So, our electrode was continuously charged and discharged over 5,000 cycles at 20 $mAcm^{-2}$ and depicted in Fig. 4(c) and its inset. With increasing the cycle number, C_s slightly decreases and retains 89.7% of its initial capacity after 5,000 cycles, indicating excellent stability for practical application. The specific capacitance and cyclic stability of $NiMoO_4$ based electrode materials are presented in

Table S1 of the Supplementary Information. For further understanding of the electrochemical behaviour, the electrochemical impedance spectrum (EIS) was carried out. Typical Nyquist plot was obtained in the frequency range of 1 Hz – 100 KHz at open circuit potential is shown in Fig. 4(d). For the battery-type electrode, the major polarization contributions are ohmic resistance (R_s), capacitance (C_{dl}) and resistive-capacitance (R_{ct}). The R_s is mainly due to the ionic resistance of the electrolyte and can be obtained from real axis intercept. The diverging spike at the low frequency region was related to the ideal capacitive contribution of the electrode (C_{dl}). Moreover, the Nyquist plot shows the converging semicircle (Fig.4d inset top right) in fourth quadrant with positive real part and negative imaginary part that may be attributed to the resistive-capacitive behaviour of the electrode [61]. In accordance with the proposed equivalent circuit (Fig. 4(d) inset down right), the diameter of the semicircle corresponds to the charge transfer resistance (R_{ct}) which arises from the surface redox reaction and is 0.18 Ω. Interestingly, the electrode exhibits a low charge transfer resistance (0.24 Ω) even after 5,000 cycles, suggesting a high electrical conductivity of the electrode, which is supported by the Mo and conductive NF [59]. This impedance spectrum results demonstrate that the honeycomb structured β-$NiMoO_4$-NF may be an excellent battery-type characteristic electrode for supercapattery.

In order to evaluate the practical application of β-$NiMoO_4$-NF as a supercapattery electrode material, a symmetric cell was fabricated with β-$NiMoO_4$-NF as positive electrode and negative electrodes. The mass ratio of negative and positive electrodes was kept to be 1:1. In the two electrode system, the energy storage is directly related to the individual electrode potential. For symmetric system, it is more complicated though both electrodes are similar; because at a high potential, the electrode kinetics could be different for individual electrodes, which could result in partial mechanical destruction, different charging voltages, etc. and thus leads to poor device performance [62]. So, the stable potential window in the symmetric cell is needed to be fixed. Generally, two electrode systems are investigated without reference electrode and thereby controlling the individual electrode potential is difficult [59]. Hence, the CV measurement was carried out with SCE as a reference electrode for as fabricated β-$NiMoO_4$-NF ‖ β-$NiMoO_4$-NF symmetric supercapattery. Figure 5(a) displays the CV curves of the symmetric cell at different scan rate of 5 – 50 mVs^{-1}, indicating that the cell is symmetrically responded for both positive and negative electrode. Both the anodic and cathodic polarizations showed redox peaks and confirming battery like energy storage process. As can be observed from CV graph, the cell can be operated up to ~1.5 V, which was fixed as a stable potential limit of the device. Typical

charge/discharge profile up to 1.5 V at various current densities ranging from 1 – 10 $mAcm^{-2}$ is shown in Fig. 5(b). The observed non-capacitive type charge-storage behaviour further supports the CV results. From charge/discharge profile, the specific capacity of the symmetric cell was evaluated using the equation (6), here the total mass of the device (~ 0.72 g) was used including electrodes, separator and packing material (para film). The obtained specific capacity for the device is found to be 50.6, 41.8, 38.3, 35.8, 32.4 and 29.3 $mAhg^{-1}$ at a current density of 1, 2, 3, 4, 6 and 10 $mAcm^{-2}$, respectively. The corresponding specific capacitances are 121.5, 100.4, 92, 86, 77.8 and 70.3 Fg^{-1} for the same current densities. The device exhibits 57.8% capacity retention when the current increases to 10 times. Noteworthy, the measured specific capacitance is 12 times higher than the $ZnCo_2O_4$ based spiral symmetric supercapacitor, which has shown 10.9 Fg^{-1} [63]. Also, it is 1.8 times higher than our previous work based on NiO-In_2O_3 (67.6 F g-1) heterostructured supercapattery [59]. Moreover, our device outperforms when compared to the reported $NiMoO_4$ based asymmetric supercapacitors such as $NiMoO_4 \cdot xH_2O \| AC$ (96.7 F g^{-1}) [64], and β-$NiMoO_4$-$CoMoO_4 \cdot xH_2O \| AC$ (80 F g^{-1}) [65]. To further investigate the electrochemical stability of the device, the cyclic performance was examined at 10 $mAcm^{-2}$ for 5,000 cycles as shown in Fig. 5(c). It is worth pointing out that the specific capacity retention is 82.9% even after 5,000 cycles, suggesting an excellent stability of the device for long term applications. It is well-known that the specific energy (E_s) and specific power (P_s) are the two important parameters for real supercapattery devices. Since the device showed a battery-like characteristics, the E_s and P_s were estimated from charge-discharge profile at different current densities using the equations (7) and (8) [59]:

$$E_s = \frac{I \int_{t=0}^{t=t} V(t)dt}{3600 \times m} \quad (7)$$

$$P_s = E/t \quad (8)$$

Here, E_S is the specific energy (Wh kg^{-1}), P_s is the specific power (W kg^{-1}), I is the specific current (Ag^{-1}), m is the mass of the device (kg), V is the potential (V) and t is discharge time (s). The Ragone plot (Energy vs. Power) shown in Fig. 5(d) compares the specific energy and power performance of the fabricated symmetric cell with recent reports. The maximum energy density of the device is 35.8 $Whkg^{-1}$ and decrease to 21.3 $Whkg^{-1}$ for 1 $mAcm^{-2}$ and 10 $mAcm^{-2}$ applied current densities, respectively. The corresponding specific power of the device is 981.56 Wkg^{-1} at 1 $mAcm^{-2}$ and increased to a maximum of 19282.4 Wkg^{-1} for a 10 $mAcm^{-2}$ current density. These values are much higher than most of the symmetric supercapatteries reported so far in the literature such as NiF_2@Ni$\|$$NiF_2$@Ni (31 Wh m^{-2}) [55],

NPC|H_2SO_4|NPC (10.86 Whkg^{-1}) [66], and PPy@MnMoO4‖PPy@$MnMoO_4$ (34.4 Whkg^{-1}) [67]. Furthermore, the two devices connected in series to light up a red LED (~3 V) during discharge as shown in Fig. 5(c inset), demonstrates the real life usability of the device. The ion-transfer kinetics was further evaluated with electrochemical impedance spectra analysis after the 1st and 5,000 charge/discharge cycles and the detailed analysis is provided in the SI section. The superior electrochemical performance may be due to the following reasons: the interconnected nanosheets increase the electrode/electrolyte contact area and provide more active sites for fast redox reactions. Open network honeycomb like architecture enhances the volume space to accommodate more electrolyte ions and increases the rate performance and cyclic stability. The strong NF foam support validates the mechanical stability and fast electron transfer pathway for the device that offers a high energy and power density. As a result, it can be concluded that the β-$NiMoO_4$-NF with interesting honeycomb microstructure could be better choice as both positive and negative electrode for next generation supercapatteries.

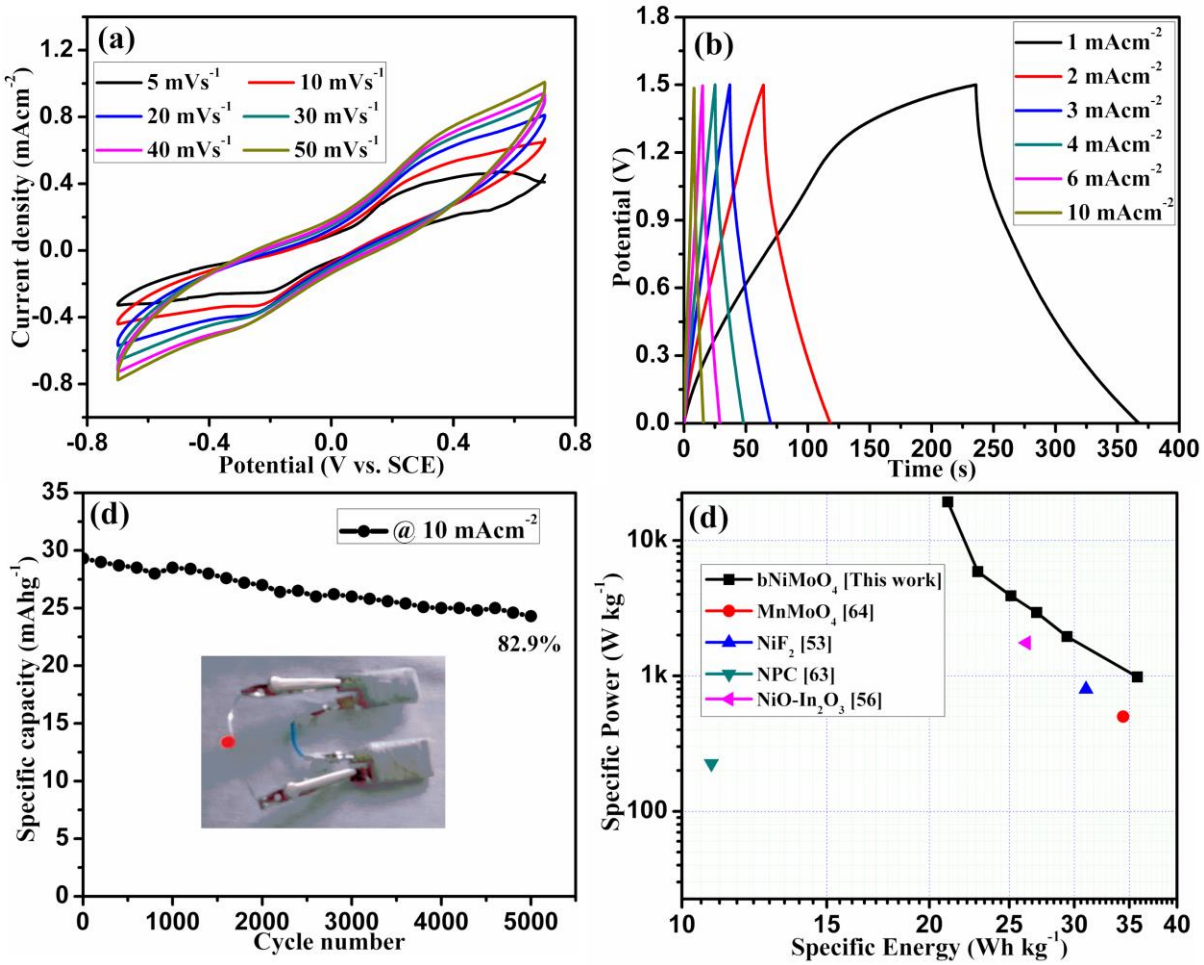


Fig. 5 (a) CV curves of symmetric cell at different scan rate, (b) Charge/discharge profile of the symmetric cell measured at different current densities (c) Cyclic stability of the β-$NiMoO_4$-

NF Supercapatteries and (d) Ragone plot of the symmetric cell and comparison with reported values.

3.3.2 Methanol Oxidation

The electro-oxidation of methanol for honeycomb like β-$NiMoO_4$-NF catalyst is evaluated within the alkaline medium. Figure 6(a) represents the CV curves of β-$NiMoO_4$-NF catalyst in 1 M KOH and 1 M KOH + 1 M CH_3OH solutions at a 5 mV s^{-1} scan rate. In 1 M KOH solution, the CV curve evidences a pair of redox peaks in the potential range of -0.1 to 0.5 V, which confirms the redox process at the electrode surface. With methanol addtion, the anodic peak current suddenly increased due to the electro-oxidation of methanol by the β-$NiMoO_4$-NF catalyst via the conversion mechanism (9) – (11) as reported earlier [68]:

$$Ni^{2+}MoO_4 + 2OH^- \rightarrow Ni(OH)_2MoO_4 + 2e^- \quad (9)$$

$$Ni(OH)_2 \rightarrow NiOOH + H^+ + e^- \quad (10)$$

$$NiOOH + CH_3OH \rightarrow Ni(OH)_2 + oxidation\ products\ of\ methanol \quad (11)$$

Conversely, the corresponding cathodic peak current decreases during the reverse sweep. The methanol oxidation current density is 41.78 mA/cm^2 for the β-$NiMoO_4$-NF catalyst at the maximum potential of 0.5 V and shows a low onset potential of ~0.29 V. Interestingly, for β-$NiMoO_4$-NF catalyst, it is one of the smallest onset potentials observed as compared to the reported value of 0.42 V [33], indicating the applicability of β-$NiMoO_4$-NF electrocatalyst for the DMFCs. A maximum current density of 41.78 mA/cm^2 was measured, which is comparatively higher than the earlier reported value of 31.18 mA/cm^2 [33]. These results evidence the superior electrocatalytic performance of the β-$NiMoO_4$-NF micro/nanostructure for methanol oxidation. During electro-oxidation, methanol fuel reacts with NiOOH electro-active compound over the catalyst surface and thereby the peak current varied in both positive and negative sweeps. In order to investigate the scan rate dependent electrocatalytic activity, the CV curves measured at different scan rates ranging from 5 to 50 mV s^{-1} is shown in Fig. 6(b). When the scan rate increases, the oxidation current also increases considerably thus further confirming the superior electron transfer kinetics within the catalyst [69]. The peak anodic current does not deviate greatly even with higher scan rate (50 mVs^{-1}) when compared to lower scan rate (5 mVs^{-1}), indicative of excellent electrocatalytic activity in this type of electrode.

The long term catalytic stability of β-$NiMoO_4$-NF towards methanol oxidation was investigated by repeated cyclic voltammogram at a scan rate of 50 mV s^{-1} over 1,000 cycles. Figure 6(c) shows the representative CVs for the first and after 1,000 cycles. A current density of 25.07 $mAcm^{-2}$ was observed after 1,000 cycles indicating good electrical conductivity of the electrode. The electrode could retain more than 58% catalytic activity even after 1,000 cycles, demonstrating good stability of the catalyst. The chronoamperometric response for a prolonged time of 3,000 s measured at 0.5 V is shown in Fig. 6(d). After the initial drop in current in the first 70 s, a stable current of 38.6 mA/cm^2 was measured for up to 1000 s, and showed a current of 36.2 mA/cm^2 (~87.4% of initial current) at 3000 s, indicating good stability of this honeycomb microstructure. The amperometric response after 1,000 CV (Fig. 6(d) inset) cycles further reveals the long term durability of the catalyst. The slight fluctuation (150 – 300 s) in the amperometric curve reveals the impact of the generated oxidation products (i.e. CO, CO_2, etc.) of methanol [70]. Further evaluation of methanol oxidation process using EIS spectra analysis before and after cyclic performance has been described in detail in the SI section.

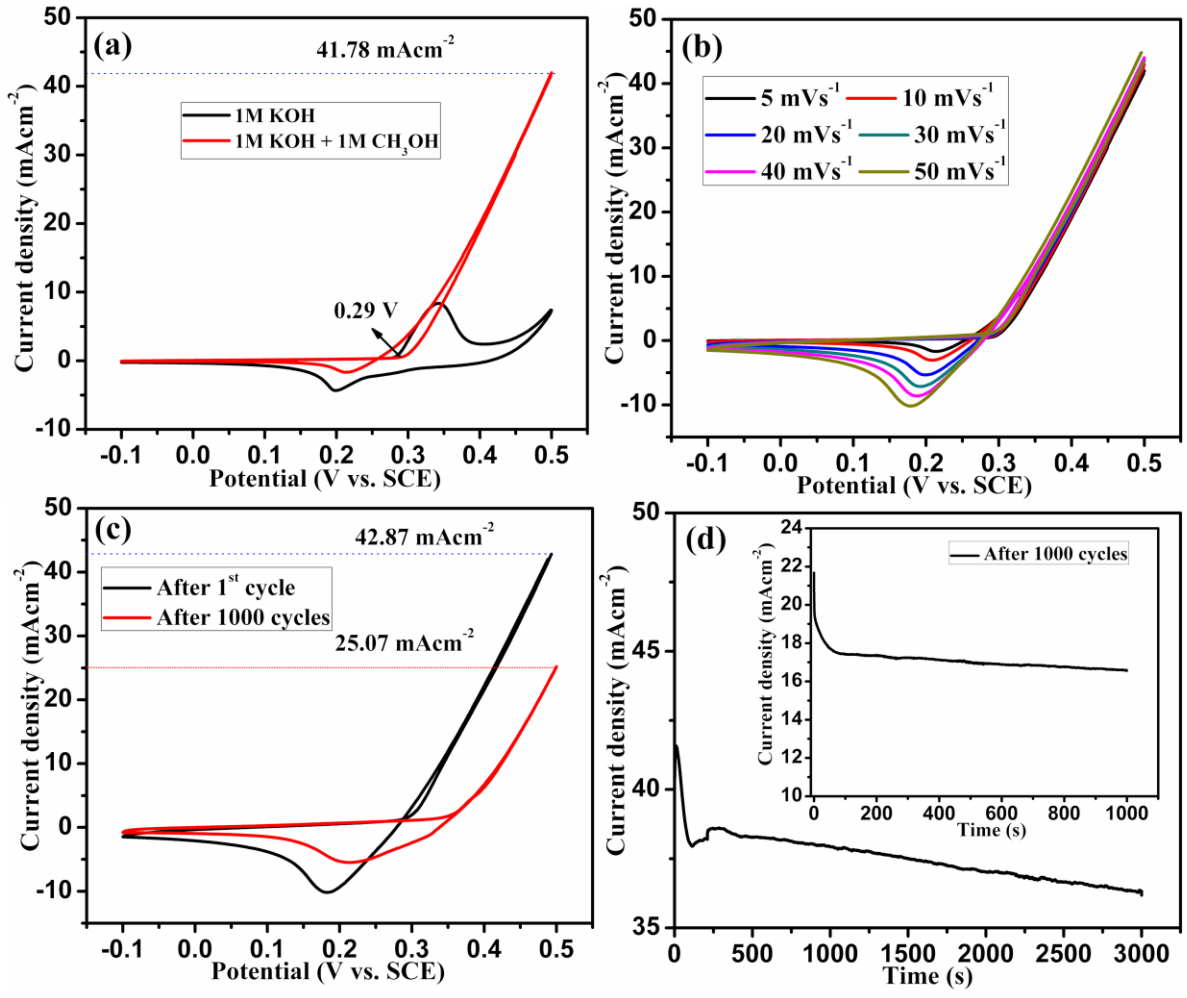


Fig. 6 (a) CV curve of β-$NiMoO_4$-NF without and with 1 M CH3OH at 5 mVs^{-1}, (b) Electro-oxidation of methanol at various scan rates, (c) Cyclic stability of the catalyst after 1000 cycles at 50 mVs^{-1} and (d) Amperometric response of catalyst after 1st cycle and after 1000 cycles (inset) at 0.5 V.

The effective use of $NiMoO_4$-NF electro-catalyst in the real metric DMFC application requires an understanding of the issues related to this electro-catalyst. Typical DMFC performance is associated with the combination of methanol oxidation reaction (MOR @ cathode) and oxygen reduction reaction (ORR @ anode) as suggested in equations (12) and (13) [71]:

$$CH_3OH + H_2O \xrightarrow{MOR} CO_2 + 6H^+ + 6e^- \quad (12)$$

$$O_2 + 4H^+ + 4e^- \xrightarrow{ORR} 2H_2O \quad (13)$$

To support these reactions, continuous oxygen supply is needed and maintained by critical air flow meter. If air flow is insufficient, the protons can migrate to cathode region and undergoes hydrogen evolution reaction (HER) as in equation (14) [72]:

$$2H^+ + 2e^- \xrightarrow{HER} H_2 \quad (14)$$

The generated hydrogen also contributes to produce current in the cathode compartment, thus HER coupled with the MOR makes complications in the device evaluation. Moreover, the MOR is directly correlated with the concentration of alkaline solution where, high alkaline concentration could reduce the over-potential, accompanying with the fast oxygen evolution reaction (OER) [73]. It further complicates the evaluation of catalyst activity and efficiency towards both MOR and OER reactions. So, it is important to know the complete characteristic nature of the electrode before take that into device fabrication. Here, the work has been further extended to study the OER and HER behaviour of $NiMoO_4$-NF in order to clarify the actual MOR for real DMFC applications. The electrochemical performances of the electrocatalyst towards the simultaneous OER and HER in alkaline medium were investigated by linear sweep voltammetry (LSV). Figure 7(a) shows the anodic polarization curves of the $NiMoO_4$-NF catalyst measured at different scan rates (5 – 100 mVs^{-1}) over the potential range of -1 to 1 V vs. SCE. Both electrochemical processes (OER & HER) at the electrode surface can be observed. To represent the potential versus reversible hydrogen electrode (RHE from SCE potential), (15) and (16) equations are used for conversion [74]:

For OER $E_{RHE} = E_{SCE} + 0.244 + 0.059 \times pH$ (pH = 13 @ 1 M KOH) (15)

For HER $E_{RHE} = E_{SCE} + E^{0}_{SCE}$ (16)

The overpotential is calculated using the relation, $\eta = E_{RHE} - 1.23$ V and $\eta = E_{RHE} + E^{0}_{SCE}$ for OER and HER respectively [75]. The *iR* compensation of current was measured using Ohmic resistance (R_s) as measured from EIS spectra as shown in Fig. S6(b). The LSV polarization curve of $NiMoO_4$-NF in OER reaction at 5 mVs^{-1} is shown in Fig. 7(b). The anodic peaks around 1.4 − 1.5 V versus RHE are ascribed to oxidation of Ni^{2+} to Ni^{3+} which can enhance the amount of active sites for HER electrocatalyst activity. When the current density is 10 $mAcm^{-2}$, the onset potential is 1.581 V vs. RHE and the corresponding overpotential is found to be 351 mV for OER. This value is comparable with the different catalysts as reported elsewhere and presented in Table S2 (Supplementary Information). Tafel plot is also used to analyse the kinetics of the catalyst and shown in Fig. 7(b) inset. As can be obtained from the Tafel plot, the slope is about 256 $mVdec^{-1}$, which is higher than the commercial RuO_2 catalyst. This could be explained by the formation of surface redox couples on the catalyst surface that acts as a barrier for OER and thereby high overpotential and Tafel slope were observed. Considering the hydrogen evolution reaction, the Fig. 7(c) shows the polarization curve at 5 mVs^{-1} vs. RHE. The $NiMoO_4$-NF exhibits reasonable catalytic ability and durability in a 1 M KOH. It showed overpotential of 238 mV at 10 $mAcm^{-2}$ of HER current density, which is quite lower than the related compounds as presented in Table S2 (Supplementary Information). The corresponding Tafel plot (inset) reveals the catalyst have a low slope of 67 $mVdec^{-1}$, implies the faster kinetics for HER [75]. Furthermore, to evaluate the durability of the catalyst for OER and HER activities, the amperometric response was carried out for nearly 19 h and shown in Fig. 7(d). Here, the current density increases for first few hours and then gradually decreases, which is mainly associated to the activation of catalyst and strong redox reaction at the surface because of the availability of more surface redox couples [74]. After few hours of catalytic reactions, the active sites reduced and results the decrease in current density and shows reasonable stability of 71% after 19 h reaction. This result is in agreement with the observed OER/HER reaction overpotential and Tafel slope values. Thereby, it can be concluded that $NiMoO_4$-NF could be a highly desirable candidate for methanol oxidation. Also, this honeycomb like $NiMoO_4$-NF can be used as catalyst for OER/HER in water splitting reaction for hydrogen production.

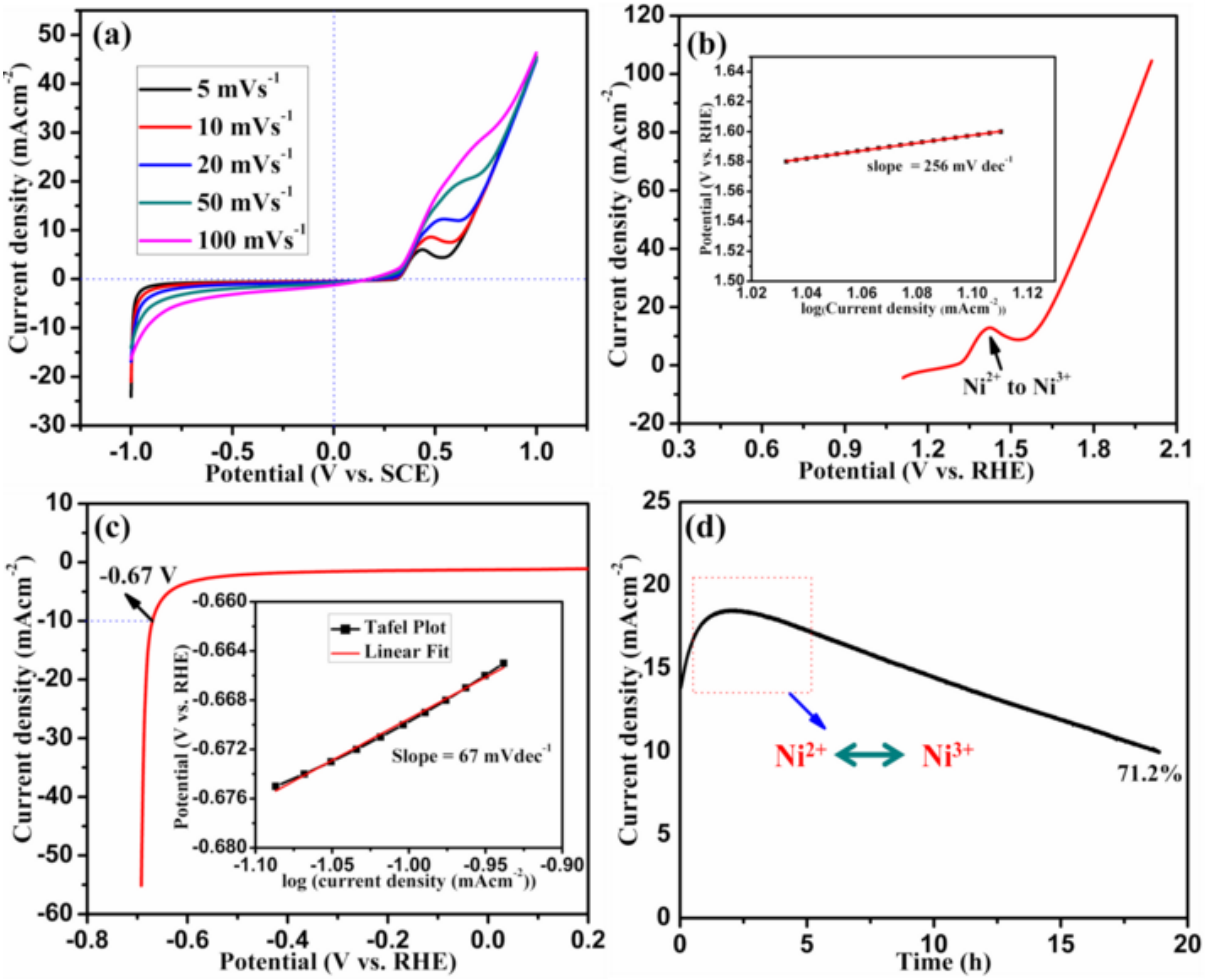


Fig. 7 (a) LSV curve of $NiMoO_4$-NF at different scan rates in 1 M KOH, (b) OER polarization curve at 5 mVs^{-1} vs RHE and the corresponding Tafel slope (inset) at near onset potential, (c) HER polarization curve at 5 mVs^{-1} vs RHE and its Tafel slope (inset) and (d) Amperometric curve at OER onset potential for 19 h.

4. Conclusions

In conclusion, a stable β-$NiMoO_4$ on 3D nickel foam was fabricated by simple PVP-assisted hydrothermal method and investigated for sustainable energy storage and conversion devices. Interestingly, the β-$NiMoO_4$–NF honeycomb architecture exhibit multifunctional features of high energy storage ability, superior electro-oxidation of methanol and reasonable OER/HER performances in alkaline medium. When used as an electrode for supercapatteries, our electrode showed a capacity of 178.2 $mAhg^{-1}$ (916.4 F g^{-1}) at 5 $mAcm^{-2}$ with excellent rate performance up to 50 $mAcm^{-2}$. Furthermore, the fabricated symmetric supercapattery has delivered an optimum energy of 35.8 $Whkg^{-1}$ at 1 $mAcm^{-2}$ and reached a maximum specific power of 19282.44 W kg^{-1} at 10 $mAcm^{-2}$. For methanol electro-oxidation, the β-$NiMoO_4$–NF

honeycomb architecture shows very low onset potential of 0.29 V with a high current density and good stability. To further extent, this interesting micro/nano structure exposed their considerable catalytic performance in OER/HER activity. At a current density of 10 $mAcm^{-2}$, it showed relatively low overpotentials of 351 and 238 mV for OER and HER, respectively. Our research results demonstrate that β-$NiMoO_4$–NF could be a more suitable multifunctional electrode/catalyst for next generation high performance energy storage and conversion devices.

Supplementary Information: XRD pattern of $NiMoO_4$-NF, EDS spectrum, Square root of scan rate vs anodic peak current plot, log I_{pa} vs. log v, square root of scan rate vs. I_{pa}/square root of the scan rate and Ratio of faradaic current and capacitive current plot, High current density charge/discharge curve, Specific capacity variation at different current densities, EIS spectra of symmetric cell before and after 5,000 cycles, EIS spectra of $NiMoO_4$-NF against methanol oxidation, and HER/OER overpotential comparison table are available.

Acknowledgement:

This work has received funding from the European Union's Horizon 2020-funded project under grant agreement no. 825114 (SmartVista).

Conflict of Interest:

There is no conflict of Interest.

107631

References

[1] Bhanvase BA, Pawade VB. Advanced Nanomaterials for Green Energy. 2018:457-72.
[2] Huang Y, Zhu M, Huang Y, Pei Z, Li H, Wang Z, et al. Multifunctional Energy Storage and Conversion Devices. Adv Mater. 2016;28:8344-64.
[3] Nitta N, Wu F, Lee JT, Yushin G. Li-ion battery materials: present and future. Materials Today. 2015;18:252-64.
[4] Kim T, Song W, Son D-Y, Ono LK, Qi Y. Lithium-ion batteries: outlook on present, future, and hybridized technologies. Journal of Materials Chemistry A. 2019;7:2942-64.
[5] Wang Y, Song Y, Xia Y. Electrochemical capacitors: mechanism, materials, systems, characterization and applications. Chem Soc Rev. 2016;45:5925-50.
[6] Zhang Y, Feng H, Wu X, Wang L, Zhang A, Xia T, et al. Progress of electrochemical capacitor electrode materials: A review. International Journal of Hydrogen Energy. 2009;34:4889-99.
[7] Chen GZ. Supercapacitor and supercapattery as emerging electrochemical energy stores. International Materials Reviews. 2016;62:173-202.
[8] Yu L, Chen GZ. Supercapatteries as High-Performance Electrochemical Energy Storage Devices. Electrochemical Energy Reviews. 2020.
[9] Bron M, Roth C. Chapter 10 - Fuel Cell Catalysis from a Materials Perspective. In: Suib SL, editor. New and Future Developments in Catalysis. Amsterdam: Elsevier; 2013. p. 271-305.

[10] Basu S. Future Directions of Fuel Cell Science and Technology. In: Basu S, editor. Recent Trends in Fuel Cell Science and Technology. New York, NY: Springer New York; 2007. p. 356-65.
[11] Akinwolemiwa B, Chen G. Fundamental Consideration for Electrochemical Engineering of Supercapattery. Journal of the Brazilian Chemical Society. 2018.
[12] Chen K, Xue D. Colloidal paradigm in supercapattery electrode systems. Nanotechnology. 2018;29:024003.
[13] Yu F, Zhang C, Wang F, Gu Y, Zhang P, Waclawik ER, et al. A zinc bromine "supercapattery" system combining triple functions of capacitive, pseudocapacitive and battery-type charge storage. Materials Horizons. 2020;7:495-503.
[14] Aricò AS, Baglio V, Antonucci V. Direct Methanol Fuel Cells: History, Status and Perspectives. Electrocatalysis of Direct Methanol Fuel Cells. 2009:1-78.
[15] Wang M, Wang X, Chen M, Yang Z, Dong C. Nanostructured electrocatalytic materials and porous electrodes for direct methanol fuel cells. Chinese Journal of Catalysis. 2016;37:1037-48.
[16] Wang C-Y. Principles of Direct Methanol Fuel Cells for Portable and Micro Power. In: Kakaç S, Pramuanjaroenkij A, Vasiliev L, editors. Mini-Micro Fuel Cells. Dordrecht: Springer Netherlands; 2008. p. 235-42.
[17] Kamarudin SK, Achmad F, Daud WRW. Overview on the application of direct methanol fuel cell (DMFC) for portable electronic devices. International Journal of Hydrogen Energy. 2009;34:6902-16.
[18] Al M, Gualous H, Omar N, Van J. Batteries and Supercapacitors for Electric Vehicles. 2012.
[19] Karaoğlan MU, İnce AC, Colpan CO, Glüsen A, Kuralay NS, Müller M, et al. Simulation of a hybrid vehicle powertrain having direct methanol fuel cell system through a semi-theoretical approach. International Journal of Hydrogen Energy. 2019;44:18981-92.
[20] Li L, Huang Z, Li H, Lu H. A High-Efficiency Voltage Equalization Scheme for Supercapacitor Energy Storage System in Renewable Generation Applications. Sustainability. 2016;8:548.
[21] Liu H, Song C, Zhang L, Zhang J, Wang H, Wilkinson DP. A review of anode catalysis in the direct methanol fuel cell. Journal of Power Sources. 2006;155:95-110.
[22] Zhang K, Han X, Hu Z, Zhang X, Tao Z, Chen J. Nanostructured Mn-based oxides for electrochemical energy storage and conversion. Chem Soc Rev. 2015;44:699-728.
[23] Sugimoto W. Ruthenium Oxides as Supercapacitor Electrodes. In: Kreysa G, Ota K-i, Savinell RF, editors. Encyclopedia of Applied Electrochemistry. New York, NY: Springer New York; 2014. p. 1813-21.
[24] Iqbal S, Khatoon H, Hussain Pandit A, Ahmad S. Recent development of carbon based materials for energy storage devices. Materials Science for Energy Technologies. 2019;2:417-28.
[25] Ramli ZAC, Kamarudin SK. Platinum-Based Catalysts on Various Carbon Supports and Conducting Polymers for Direct Methanol Fuel Cell Applications: a Review. Nanoscale research letters. 2018;13:410.
[26] Ozkan US, Kueller RF, Moctezuma E. Methanol oxidation over nonprecious transition metal oxide catalysts. Industrial & Engineering Chemistry Research. 1990;29:1136-42.
[27] Cheng K, Yang F, Ye K, Li Y, Yang S, Yin J, et al. Facile preparation of transition metal oxide–metal composites with unique nanostructures and their electrochemical performance as energy storage material. Journal of Materials Chemistry A. 2013;1:14246.
[28] Thrane J, Lundegaard LF, Beato P, Mentzel UV, Thorhauge M, Jensen AD, et al. Alkali Earth Metal Molybdates as Catalysts for the Selective Oxidation of Methanol to Formaldehyde—Selectivity, Activity, and Stability. Catalysts. 2020;10:82.
[29] Zhang L, Zheng S, Wang L, Tang H, Xue H, Wang G, et al. Fabrication of Metal Molybdate Micro/Nanomaterials for Electrochemical Energy Storage. Small. 2017;13.
[30] Kumbhar VS, Nguyen VQ, Lee YR, Lokhande CD, Kim D-H, Shim J-J. Electrochemically growth-controlled honeycomb-like NiMoO4 nanoporous network on nickel foam and its applications in all-solid-state asymmetric supercapacitors. New Journal of Chemistry. 2018;42:14805-16.
[31] Ahn JH, Park GD, Kang YC, Lee J-H. Phase-pure β-$NiMoO_4$ yolk-shell spheres for high-performance anode materials in lithium-ion batteries. Electrochimica Acta. 2015;174:102-10.

[32] Cai D, Wang D, Liu B, Wang Y, Liu Y, Wang L, et al. Comparison of the electrochemical performance of $NiMoO_4$ nanorods and hierarchical nanospheres for supercapacitor applications. ACS applied materials & interfaces. 2013;5:12905-10.
[33] Jothi PR, Kannan S, G V. Enhanced methanol electro-oxidation over in-situ carbon and graphene supported one dimensional $NiMoO_4$ nanorods. Journal of Power Sources. 2015;277:350-9.
[34] Peng S, Li L, Wu HB, Madhavi S, Lou XWD. Controlled Growth of $NiMoO_4$ Nanosheet and Nanorod Arrays on Various Conductive Substrates as Advanced Electrodes for Asymmetric Supercapacitors. Advanced Energy Materials. 2015;5:1401172.
[35] Zhang Y, Chang C-r, Jia X-d, Huo Q-y, Gao H-l, Yan J, et al. Morphology-dependent $NiMoO_4$/carbon composites for high performance supercapacitors. Inorganic Chemistry Communications. 2020;111:107631.
[36] Zhang Y, Chang C-r, Jia X-d, Cao Y, Yan J, Luo H-w, et al. Influence of metallic oxide on the morphology and enhanced supercapacitive performance of $NiMoO_4$ electrode material. Inorganic Chemistry Communications. 2020;112:107697.
[37] Yu M, Chen J, Liu J, Li S, Ma Y, Zhang J, et al. Mesoporous $NiCo_2O_4$ nanoneedles grown on 3D graphene-nickel foam for supercapacitor and methanol electro-oxidation. Electrochimica Acta. 2015;151:99-108.
[38] Zhang D, Zhang J, Wang H, Cui C, Jiao W, Gao J, et al. Novel Ni foam based nickel oxalate derived porous NiO nanostructures as highly efficient electrodes for the electrooxidation of methanol/ethanol and urea. Journal of Alloys and Compounds. 2019;806:1419-29.
[39] Zhang S, She G, Li S, Qu F, Mu L, Shi W. Enhancing the electrocatalytic activity of $NiMoO_4$ through a post-phosphorization process for oxygen evolution reaction. Catalysis Communications. 2019;129:105725.
[40] Gao W, Wang C, Ma F, Wen D. Highly active electrocatalysts of CeO_2 modified $NiMoO_4$ nanosheet arrays towards water and urea oxidation reactions. Electrochimica Acta. 2019;320:134608.
[41] Rodriguez JA, Hanson JC, Chaturvedi S, Maiti A, Brito JL. Phase transformations and electronic properties in mixed-metal oxides: Experimental and theoretical studies on the behavior of $NiMoO_4$ and $MgMoO_4$. The Journal of Chemical Physics. 1999;112:935-45.
[42] Mazzocchia C, Di Renzo F, Aboumrad C, Thomas G. Stability of β-nickel molybdate. Solid State Ionics. 1989;32-33:228-33.
[43] Brito JL, Barbosa AL, Albornoz A, Severino F, Laine J. Nickel molybdate as precursor of HDS catalysts: Effect of phase composition. Catalysis Letters. 1994;26:329-37.
[44] Kaddouri A, Anouchinsky R, Mazzocchia C, Madeira LM, Portela MF. Oxidative dehydrogenation of ethane on the α and β phases of $NiMoO_4$. Catalysis Today. 1998;40:201-6.
[45] Naik KK, Ratha S, Rout CS. Phase and Shape Dependent Non–enzymatic Glucose Sensing Properties of Nickel Molybdate. ChemistrySelect. 2016;1:5187-95.
[46] Bankar PK, Ratha S, More MA, Late DJ, Rout CS. Enhanced field emission performance of NiMoO4 nanosheets by tuning the phase. Applied Surface Science. 2017;418:270-4.
[47] Abdel-Dayem HM. Dynamic Phenomena during Reduction of α-$NiMoO_4$ in Different Atmospheres: In-Situ Thermo-Raman Spectroscopy Study. Industrial & Engineering Chemistry Research. 2007;46:2466-72.
[48] Ratha S, Samantara AK, Singha KK, Gangan AS, Chakraborty B, Jena BK, et al. Urea-Assisted Room Temperature Stabilized Metastable β-$NiMoO_4$: Experimental and Theoretical Insights into its Unique Bifunctional Activity toward Oxygen Evolution and Supercapacitor. ACS applied materials & interfaces. 2017;9:9640-53.
[49] Mazzocchia C, Anouchinsky R, Kaddouri A, Sautel M, Thomas G. Thermal activation of typical oxidative dehydrogenation catalyst precursors belonging to the Ni−Mo−O system. Journal of Thermal Analysis and Calorimetry. 2007;40:1253-65.
[50] Rodriguez JA, Chaturvedi S, Hanson JC, Albornoz A, Brito JL. Electronic Properties and Phase Transformations in CoMoO4 and $NiMoO_4$: XANES and Time-Resolved Synchrotron XRD Studies. The Journal of Physical Chemistry B. 1998;102:1347-55.

[51] Kadam SR, Late DJ, Panmand RP, Kulkarni MV, Nikam LK, Gosavi SW, et al. Nanostructured 2D MoS2 honeycomb and hierarchical 3D $CdMoS_4$ marigold nanoflowers for hydrogen production under solar light. Journal of Materials Chemistry A. 2015;3:21233-43.
[52] Soligno G, Vanmaekelbergh D. Understanding the Formation of PbSe Honeycomb Superstructures by Dynamics Simulations. Physical Review X. 2019;9:021015.
[53] Chavan HS, Hou B, Ahmed ATA, Jo Y, Cho S, Kim J, et al. Nanoflake $NiMoO_4$ based smart supercapacitor for intelligent power balance monitoring. Solar Energy Materials and Solar Cells. 2018;185:166-73.
[54] Shinde PV, Shinde NM, Yun JM, Mane RS, Kim KH. Facile Chemical Synthesis and Potential Supercapattery Energy Storage Application of Hydrangea-type Bi2MoO6. ACS Omega. 2019;4:11093-102.
[55] Shinde NM, Shinde PV, Yun JM, Gunturu KC, Mane RS, O'Dwyer C, et al. NiF2 Nanorod Arrays for Supercapattery Applications. ACS Omega. 2020;5:9768-74.
[56] Sankar KV, Seo Y, Lee SC, Liu S, Kundu A, Ray C, et al. Cobalt carbonate hydroxides as advanced battery-type materials for supercapatteries: Influence of morphology on performance. Electrochimica Acta. 2018;259:1037-44.
[57] Kim H-S, Cook JB, Lin H, Ko Jesse S, Tolbert Sarah H, Ozolins V, et al. Oxygen vacancies enhance pseudocapacitive charge storage properties of MoO_{3-x}. Nature Materials. 2017;16:454-60.
[58] Tang N, You H, Li M, Chen GZ, Zhang L. Cross-linked $Ni(OH)_2/CuCo_2S_4$/Ni networks as binder-free electrodes for high performance supercapatteries. Nanoscale. 2018;10:20526-32.
[59] Padmanathan N, Shao H, McNulty D, O'Dwyer C, Razeeb KM. Hierarchical $NiO–In_2O_3$ microflower (3D)/ nanorod (1D) hetero-architecture as a supercapattery electrode with excellent cyclic stability. Journal of Materials Chemistry A. 2016;4:4820-30.
[60] Kannan V, Kim HJ, Park HC, Kim HS. Single-Step Direct Hydrothermal Growth of $NiMoO_{(4)}$ Nanostructured Thin Film on Stainless Steel for Supercapacitor Electrodes. Nanomaterials. 2018;8:563.
[61] Danzer AM. Generalized Distribution of Relaxation Times Analysis for the Characterization of Impedance Spectra. Batteries. 2019;5:53.
[62] Borenstein A, Attias R, Hanna O, Luski S, Kaner RB, Aurbach D. A Surprising Failure Mechanism in Symmetric Supercapacitors at High Voltages. ChemElectroChem. 2017;4:2660-8.
[63] Wu H, Lou Z, Yang H, Shen G. A flexible spiral-type supercapacitor based on $ZnCo_2O_4$ nanorod electrodes. Nanoscale. 2015;7:1921-6.
[64] Liu M-C, Kang L, Kong L-B, Lu C, Ma X-J, Li X-M, et al. Facile synthesis of $NiMoO_4·xH_2O$ nanorods as a positive electrode material for supercapacitors. RSC Advances. 2013;3:6472-8.
[65] Senthilkumar B, Meyrick D, Lee Y-S, Selvan RK. Synthesis and improved electrochemical performances of nano β-$NiMoO_4$–$CoMoO_4·xH_2O$ composites for asymmetric supercapacitors. RSC Advances. 2013;3:16542-8.
[66] Salunkhe RR, Kamachi Y, Torad NL, Hwang SM, Sun Z, Dou SX, et al. Fabrication of symmetric supercapacitors based on MOF-derived nanoporous carbons. Journal of Materials Chemistry A. 2014;2:19848-54.
[67] Wang H, Song Y, Zhou J, Xu X, Hong W, Yan J, et al. High-performance supercapacitor materials based on polypyrrole composites embedded with core-sheath polypyrrole@$MnMoO_4$ nanorods. Electrochimica Acta. 2016;212:775-83.
[68] Yi Q, Huang W, Zhang J, Liu X, Li L. Methanol oxidation on titanium-supported nano-scale Ni flakes. Catalysis Communications. 2008;9:2053-8.
[69] Prathap MUA, Satpati B, Srivastava R. Facile preparation of β-$Ni(OH)_2$-$NiCo_2O_4$ hybrid nanostructure and its application in the electro-catalytic oxidation of methanol. Electrochimica Acta. 2014;130:368-80.
[70] Gu CD, Huang ML, Ge X, Zheng H, Wang XL, Tu JP. NiO electrode for methanol electro-oxidation: Mesoporous vs. nanoparticulate. International Journal of Hydrogen Energy. 2014;39:10892-901.

[71] Kim H, Ünlü M, Zhou J, Anestis-Richard I, Kohl PA. Anionic–cationic bi-cell design for direct methanol fuel cell stack. Journal of Power Sources. 2010;195:7289-94.
[72] Ye Q, Yang X-G, Cheng P. Modeling of spontaneous hydrogen evolution in a direct methanol fuel cell. Electrochimica Acta. 2012;69:230-8.
[73] Chen D, Minteer SD. Mechanistic study of nickel based catalysts for oxygen evolution and methanol oxidation in alkaline medium. Journal of Power Sources. 2015;284:27-37.
[74] Du X, Fu J, Zhang X. $NiCo_2O_4$@$NiMoO_4$ Supported on Nickel Foam for Electrocatalytic Water Splitting. ChemCatChem. 2018;10:5533-40.
[75] Jia D, Gao H, Xing L, Chen X, Dong W, Huang X, et al. 3D Self-Supported Porous NiO@$NiMoO_4$ Core–Shell Nanosheets for Highly Efficient Oxygen Evolution Reaction. Inorganic Chemistry. 2019;58:6758-64.